# Fault-Free Integrity and Continuity for Driverless Urban Vehicle Navigation with Multi-sensor Integration: A Case Study in Downtown Chicago

Kana Nagai, Matthew Spenko, Ron Henderson, Boris Pervan, *Illinois Institute of Technology*

## BIOGRAPHY

**Kana Nagai** is currently a Ph.D. candidate and Research Assistant in Mechanical and Aerospace Engineering at Illinois Institute of Technology (IIT). She received her B.S. in Mechanical Engineering from IIT and B.E. in Architecture from Hokkaido University, Japan.

**Dr. Matthew Spenko** is a Professor of Mechanical and Aerospace Engineering at Illinois Institute of Technology. He earned his B.S. degree in Mechanical Engineering from Northwestern University and M.S. and Ph.D. degrees in Mechanical Engineering from the Massachusetts Institute of Technology. He was an Intelligence Community postdoctoral fellow working at Stanford University in the Mechanical Engineering Department.

**Ron Henderson FASLA** is Professor and Director of the Landscape Architecture + Urbanism Program at Illinois Institute of Technology. He is founding principal of LIRIO Landscape Architecture, Senior Fellow at Dumbarton Oaks, and a Japan-US Creative Fellow. Prof. Henderson received his B.Arch. from University of Notre Dame and his Master of Landscape Architecture and Master of Architecture from University of Pennsylvania.

**Dr. Boris Pervan** is a Professor of Mechanical and Aerospace Engineering at Illinois Institute of Technology, where he conducts research on advanced navigation systems. Prior to joining the faculty at IIT, he was a spacecraft mission analyst at Hughes Aircraft Company (now Boeing) and a postdoctoral research associate at Stanford University. Prof. Pervan received his B.S. from the University of Notre Dame, M.S. from the California Institute of Technology, and Ph.D. from Stanford University.

## ABSTRACT

Driverless vehicles must operate with a safety integrity level, but urban environments degrade GNSS navigation accuracy and thereby fault-free integrity. Integration with INS helps maintain continuity, but position errors drift over time without GNSS signals. Whether modern navigation systems can provide satisfactory integrity for driverless vehicles throughout a city is still undetermined. This research investigates how GNSS and INS, when appropriately augmented by LiDAR ranging from local landmarks, can safely navigate vehicles through a real-world urban environment. We begin by defining safety requirements for driverless vehicles under fault-free conditions and developing measurement models for multi-sensor integrated navigation systems using an EKF. The critical elements of urban navigation are then discussed, including individual INS noise parameter specifications and the effect of velocity updates. Simulations along a nine-kilometer-long urban transect in downtown Chicago show that velocity updates can extend navigation continuity by bridging intermittent GNSS signal availability. However, position reference updates at 35-meter intervals, in our case LiDAR ranges from local landmarks, are needed to achieve 100% navigation availability through the transect.

## I. INTRODUCTION

Driverless vehicles will need to operate with integrity levels on local and residential streets subject to corresponding accuracies at the centimeter-level (Reid et al., 2019). GNSS Real-Time Kinematic (RTK) positioning makes this feasible under open-sky environments, but many local and residential streets are surrounded by buildings that cause limited satellite visibility and significant multipath effects. The fact that urban environments degrade GNSS navigation performance is well-known, and the challenge of urban navigation has been investigated in previous studies.

The performance metrics of accuracy, integrity, continuity, and availability have been used to define navigation requirements for aviation for decades (Davis and Kelly, 1993) and, more recently, have been extended into land applications in urban environments (Zhu et al., 2018). A useful preliminary set of requirements applicable to future driverless vehicles operating on local and residential streets is provided in (Reid et al., 2019).

Exclusion of reflected GNSS signals is essential for integrity in urban road environments (Cosmen-Schortmann et al., 2008). 3D environment maps provide the means to trace GNSS signals. The concept of ‘shadow matching’ identifies the signal blockages in urban canyons (Groves, 2011). Overlaying sky plots on a hemispherical sky view can be used to distinguish between the line of sight (LOS) and blocked signals (Chapman et al., 2002). A Householder transformation predicting reflected rays helps to identify satellite signals affected by multipath reflections (Householder, 1958), and the exclusion of the associated measurements from the position estimation process prevents accuracy from degrading (Obst et al., 2012). However, an excessive number of such exclusions comes at the cost of satellite shortages and losses of GNSS carrier phase cycle ambiguities and RTK positioning accuracy.

Integration with an inertial navigation system (INS) can help provide continuous navigation by handling the GNSS signal outages. Tightly coupled INS/GNSS using an Extended Kalman filter (EKF) provides better position estimation in urban environments (Falco et al., 2017), and an inertial measurement unit (IMU) based on micro-electro-mechanical systems (MEMS) makes INS affordable (Titterton et al., 2004). The EKF algorithm also enables the integration of wheel speed sensors, vehicle kinematic constraints, and zero velocity updates (ZUPT) (Gao et al., 2007) (Grejner-Brzezinska et al., 2002). The interaction among the sensors—INS bridging the GNSS signal outages, and GNSS calibrating the drifting INS error—ensures that centimeter level accuracy is maintained before the error increases to a critical level. If the vehicle enters GNSS denied areas, the positioning and the drift control burden will be shared with light detection and ranging (LiDAR) positioning from local landmarks (Brenner, 2009).

Multi-sensor integrated navigation systems improve position accuracy, but whether the navigation systems can provide satisfactory integrity for driverless vehicles throughout a city is still undetermined. The research investigates how GNSS and INS, when appropriately augmented by LiDAR ranging from local landmarks, can achieve navigation safely through a real-world urban environment under fault-free conditions. Additionally, we determine the critical elements of urban navigation, including individual INS noise parameter specifications and the effect of velocity updates.

The paper is laid out as follows. Section II describes navigation performance requirements for driverless vehicles and evaluates GNSS-only availability along a nine-kilometer-long urban transect in downtown Chicago. In Section III, we develop sensor measurement models and introduce a tightly coupled INS/multi-sensor integration scheme using the EKF. Section IV determines the elements critical to the reduction of urban navigation error, including individual INS noise parameter specifications, the effect of velocity updates, and local reference landmark density. In Section V, simulations are executed to demonstrate how multi-sensor navigation systems can achieve fault-free integrity in a real urban environment. The last section presents our conclusions.

## II. NAVIGATION PERFORMANCE REQUIREMENTS

### 1. Integrity

To ensure integrity, a vehicle’s horizontal positioning error is bounded by a protection level computed with respect to designated probability. Integrity can be evaluated based on whether the protection level exceeds a required alert limit. For this work, we assume driverless vehicle integrity requires that the probability of exceeding a 0.5-meter alert limit must be lower than $10^{-7}$. The 0.5-meter alert limit corresponds to approximately a 5 $\sigma$ event under fault-free conditions (Fig. 1), so the maximum allowable position error standard deviation is then approximately 0.1 meters. In the remainder of the paper, we will use the 0.1-meter ($1\sigma$) position error standard deviation as an approximate fault-free integrity evaluation threshold in both the along-track (the heading, $x$) and the cross-track (the lateral, $y$) directions.

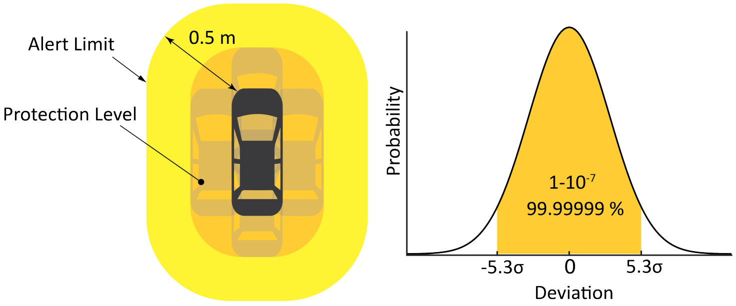

**Figure 1:** Fault-free integrity requirements used in this work.

## 2. Continuity and Availability

Fault-free integrity does not account for the duration of navigation performance since it is evaluated from the position error at the given spot and time. We express continuity as the traveled distance over which the position error standard deviation remains successively lower than 0.1 m.

The time of day also impacts navigation performance because GNSS satellite motion influences satellite visibility. We evaluate availability, the percentage of time in a day when the system provides navigation service meeting the requirements, from fault-free integrity results when the vehicle leaves the starting point every 15 minutes for 24 hours. The availability requirement is 100% as driverless vehicles will be expected to operate at any time of day as human-driven vehicles do today.

The evaluation scenario assumes the driverless vehicle enters an urban core from an open-sky starting point where it has already completed GNSS RTK cycle ambiguity initialization and INS alignment, with initial horizontal position error standard deviation <0.02 m and yaw attitude error standard deviation <0.1 deg. We evaluate the navigation performance after the initialization and alignment.

## 3. GNSS Availability in a City

We begin our analysis by evaluating availability of four GNSS constellations — GPS, Galileo, GLONASS, and BeiDou — when a driverless vehicle travels nine kilometers down State Street in Chicago in a simulated environment. The route along the street passes through a variety of environments, from low-rise, near open-sky neighborhoods to dense urban canyons with skyscrapers taller than 100 meters. High-definition 3D maps including all the streets and buildings are used for the exclusion of blocked and reflected signals (Fig. 2a).

The 3D map allows us to project the field of view from successive 10-meter waypoints onto a hemisphere representing the building occupancy in the sky. When the projection is overlapped with a sky plot of satellites, we can predict the signals from the satellites blocked by the buildings (Fig. 2b). Signals reaching a vehicle's receiver via specular reflection must be excluded as well. We use the building occupancy sky plots and Householder transformations to determine whether a hypothesized reflection ray vector actually strikes a physical wall. If the simulated ray strikes a wall, the antenna receives the reflected signal from a phantom satellite direction (Fig. 2c) (Nagai et al., 2020). Range measurements associated with blocked or reflected signals are not included in subsequent positioning calculations.

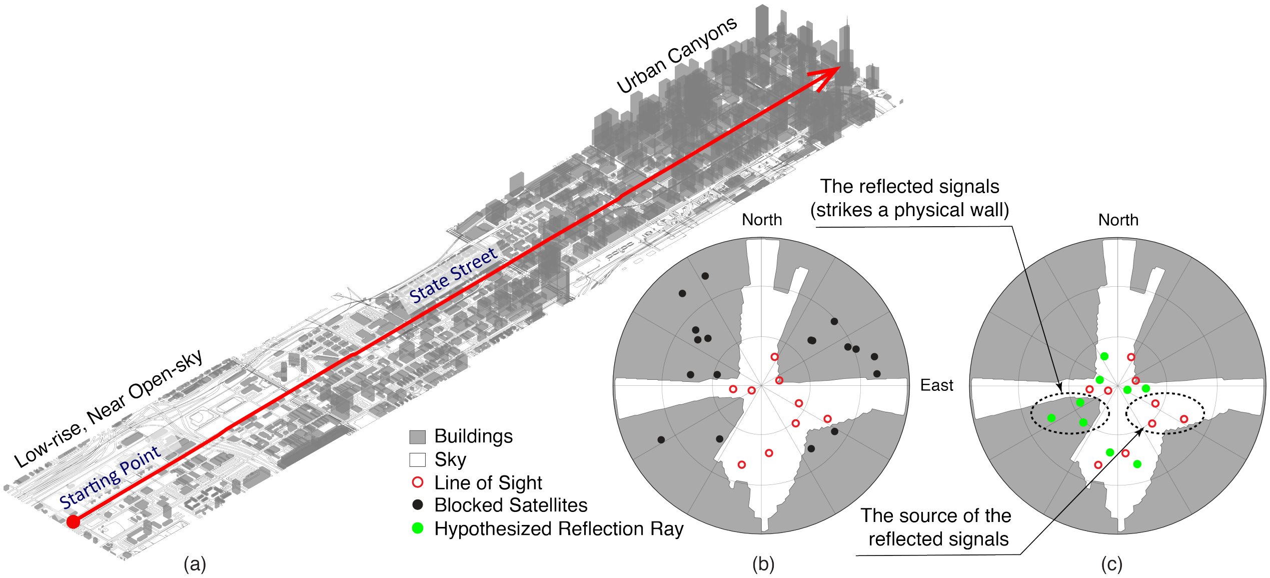

(a) (b) (c)

**Figure 2:** (a) High-definition 3D maps showing our simulation transect, State Street in Chicago; (b, c) Line of sight, blocked, and reflected signal identification

First, we evaluate GNSS satellite visibility over the street using horizontal position dilution of precision (HDOP) (Nagai et al., 2020). While GNSS user range error would fluctuate in the real world, we imagine that GNSS RTK constantly provides a nominal ranging error standard deviation of 0.02 meters. The maximum allowable HDOP is then approximately 5, given the existing assumptions of the 0.1-meter maximum allowable position error standard deviation and the 0.02-meter GNSS RTK ranging error standard deviation. Figure 3, which depicts GNSS satellite visible regions where HDOP is less than 5, shows how

GNSS satellite visibility deteriorates gradually as building height rises. We divide the environments in the figure into three (qualitative) categories: open-sky, intermittent GNSS availability, and a succession of GNSS denied areas.

Figure 4 shows GNSS availability based on the driverless vehicle integrity requirements (Nagai et al., 2021b), with availability never reaching 100% after 2000 meters. Once the vehicle passes under an overpass, all estimated integer ambiguities are reset. The GNSS RTK re-initialization is never completed to provide satisfactory accuracy, even if there is sufficient GNSS satellite visibility. The results clearly show INS is required to recover integer ambiguities between GNSS signal outages to extend navigation continuity in the urban environment.

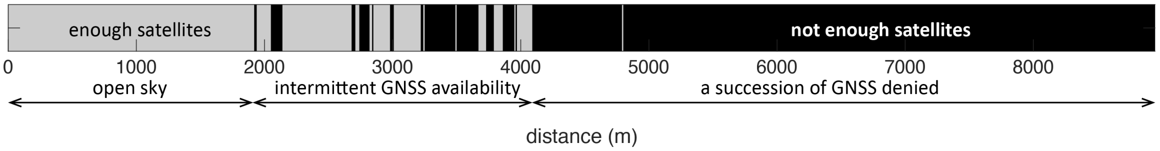

**Figure 3:** GNSS satellite visibility over State Street, Chicago based on HDOP evaluation

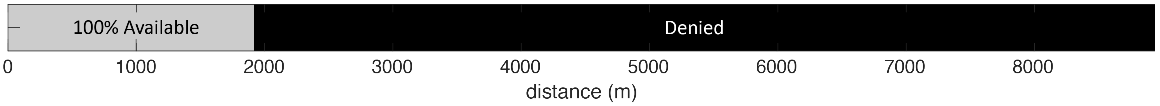

**Figure 4:** GNSS availability evaluation corresponding to the fault free integrity integrity requirements for vehicle travelling south (left) to north (right).

## III. MULTI-SENSOR INTEGRATED NAVIGATION SYSTEMS

Interaction among the sensors will extend navigation continuity, and the EKF algorithm enables measurements from multiple sensors to integrate. We investigate the integration of INS, zero velocity update (ZUPT), LiDAR, GNSS, wheel speed sensors, non-holonomic, and holonomic kinematic constraints. Figure 5 shows the multi-sensor integration architecture. The tightly coupled EKF integration utilizes the INS measurement for prediction and the other sensor measurements for observation. The observations from each sensor are incorporated through the measurement updates, and then the INS measurements and the process model generate the time updates. LiDAR is an optional sensor, and we call INS, GNSS, wheel speed sensors, vehicle dynamic constraints, and ZUPT conventional sensors.

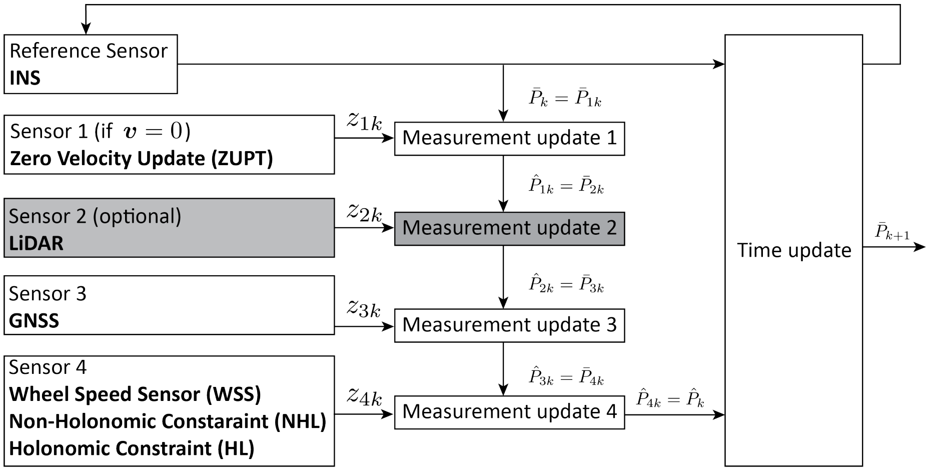

**Figure 5:** The multi-sensor integration architecture.

The INS continuous linearized dynamic model (Tanil, 2016) is described as

$$\dot{\boldsymbol{x}}_k = \boldsymbol{F}_k \boldsymbol{x}_k + \boldsymbol{G}_{uk} \boldsymbol{u}_k + \boldsymbol{G}_{wk} \boldsymbol{w}_k \tag{1}$$

where $\boldsymbol{x} = [\delta \boldsymbol{r}_N, \delta \boldsymbol{v}_N, \delta \boldsymbol{E}_N, \boldsymbol{b}_a, \boldsymbol{b}_g]^T$ is the state vector having position $\delta \boldsymbol{r}_N$ in the navigation frame, velocity $\delta \boldsymbol{v}_N$, attitude

$\delta \boldsymbol{E}_N$, and INS bias errors for the accelerometer $\boldsymbol{b}_a$ and the gyros $\boldsymbol{b}_g$. $\boldsymbol{u} = [\delta \tilde{\boldsymbol{f}}_B, \delta \tilde{\boldsymbol{\omega}}_B]^T$ is the input vector having accelerometer specific force measurement $\tilde{f}$ in the body frame and gyro rotation rate measurement $\tilde{\omega}$. $\boldsymbol{w} \sim N(0, \boldsymbol{W})$ is the white noise vector of the process model. The ZUPT measurement model is described as

$$\underbrace{[\delta \boldsymbol{v}_B (= 0)]}_{z_{1k}} = \underbrace{[0,\ {}^B\boldsymbol{R}^{N*},\ \boldsymbol{v}_B^* \times]}_{H_{1k}} \underbrace{\begin{bmatrix} \delta \boldsymbol{r}_N \\ \delta \boldsymbol{v}_N \\ \delta \boldsymbol{E}_N \end{bmatrix}}_{x_{1k}} + \boldsymbol{\nu}_{1k} \tag{2}$$

where $\delta \boldsymbol{v}_B$ is the velocity in the body frame, and $\boldsymbol{\nu}_{1k} \sim N(0, \boldsymbol{V}_{1k})$ is the vector of the velocity violation noise, modelled as white. The LiDAR measurement model (Nagai et al., 2021b) is described as

$$\underbrace{\begin{bmatrix} \boldsymbol{d}^i - \boldsymbol{d}^{i*} \\ \boldsymbol{\theta}^i - \boldsymbol{\theta}^{i*} \end{bmatrix}}_{z_{2k}} = \boldsymbol{H}_{2k} \underbrace{\begin{bmatrix} \delta \boldsymbol{r}_N \\ \delta \boldsymbol{E}_N \\ \hline \delta \boldsymbol{p}^i \end{bmatrix}}_{x_{2k}} + \boldsymbol{\Gamma}_{2k} \boldsymbol{\nu}_{2k} \tag{3}$$

where, $d^i$ is the ranging measurement of the $i^{th}$ landmark ($i = 1, 2, ..., n$), $\theta^i$ is the angle measurement, $p^i$ is landmark location in the navigation frame, and $\boldsymbol{\nu}_{2k} \sim N(0, \boldsymbol{V}_{2k})$ is the white noise vector of the LiDAR measurements. The EKF GNSS double difference measurement model (Tanil, 2016) is described as

$$\underbrace{\begin{bmatrix} \boldsymbol{\phi}^{kl} - \boldsymbol{G}^{kl} \boldsymbol{r}^* \\ \boldsymbol{\rho}^{kl} - \boldsymbol{G}^{kl} \boldsymbol{r}^* \end{bmatrix}}_{z_{3k}} = \underbrace{\left[\begin{array}{c|cc|c} \boldsymbol{G}^{kl} & \boldsymbol{\Lambda} & 0 & \lambda \mathbf{I} \\ \boldsymbol{G}^{kl} & 0 & \boldsymbol{\Lambda} & 0 \end{array}\right]}_{H_{3k}} \underbrace{\begin{bmatrix} \delta \boldsymbol{r}_N \\ \hline \boldsymbol{m}_\phi \\ \boldsymbol{m}_\rho \\ \hline \boldsymbol{N} \end{bmatrix}}_{x_{3k}} + \boldsymbol{\Gamma}_{3k} \boldsymbol{\nu}_{3k} \tag{4}$$

where $\boldsymbol{\phi}$ is the carrier phase measurement, $\boldsymbol{\rho}$ is code phase measurement, $\boldsymbol{G}$ is the observation matrix containing line of sight vectors excluding the pseudorange measurements associated with the blocked and reflected signals, $\boldsymbol{m}$ is the multipath error, and $\boldsymbol{N}$ is the integer ambiguity. $\boldsymbol{\nu}_{3k} \sim N(0, \boldsymbol{V}_{3k})$ is the white noise vector of the GNSS measurements. Wheel speed sensors are standard equipment for all vehicles, and vehicle dynamic constraints are applicable without equipment. We developed the model described in (5) consisting of wheel speed sensor measurement in the along-track direction, non-holonomic constraint resisting lateral sliding, and holonomic constraint on vertical movement (Nagai et al., 2021a).

$$\underbrace{\delta \boldsymbol{v}_B}_{z_{4k}} = \underbrace{[0,\ {}^B\mathbf{R}^{N*},\ ({}^B\mathbf{R}^{N*} \boldsymbol{v}_N^* \times + \boldsymbol{L}_B\ {}^B\mathbf{R}^{N*}\ {}^I\boldsymbol{\omega}_N^E \times),\ 0,\ \boldsymbol{L}_B,\ -\tfrac{\omega_R}{2},\ -\tfrac{\omega_L}{2}]}_{H_{4k}} \underbrace{\begin{bmatrix} \boldsymbol{x}_k \\ \delta R_R \\ \delta R_L \end{bmatrix}}_{x_{4k}} - \boldsymbol{L}_B \delta^I \tilde{\boldsymbol{\omega}}_B^B + \boldsymbol{\Gamma}_{4k} \boldsymbol{\nu}_{4k} \tag{5}$$

where $\boldsymbol{R}$ is the rotation matrix, $\boldsymbol{L}_B$ is the skew-symmetric matrix form of distance between the center of mass and the wheel axis, ${}^I\boldsymbol{\omega}_N^E$ is the earth rotation rate, $w_R, w_L$ are the measurements vector of a wheel rotation rate obtained from the wheel speed sensors, and $\delta R_R, \delta R_L$ are the radius of the wheels. $\boldsymbol{\nu}_{4k} \sim N(0, \boldsymbol{V}_{4k})$ is the white noise vector of the wheel speed sensor measurements. Both (2) and (5) measure the velocity of the body frame, but (2) is used only when the vehicle is stationary.

We use the state error covariance for the integrity analysis. The EKF error covariance matrix propagation is described as

$$\hat{\boldsymbol{P}}_k = (\mathbf{I} - \boldsymbol{K}_k \boldsymbol{H}_k) \bar{\boldsymbol{P}}_k \tag{6}$$

$$\bar{\boldsymbol{P}}_{k+1} = \boldsymbol{\Phi}_k \hat{\boldsymbol{P}}_k \boldsymbol{\Phi}_k^T + \boldsymbol{Q}_k \tag{7}$$

where $\hat{\boldsymbol{P}}$ is the updated estimate covariance, $\boldsymbol{K}$ is the Kalman gain, $\bar{\boldsymbol{P}}$ is the predicted estimate covariance, $\boldsymbol{\Phi}$ is the state transition matrix, and $\boldsymbol{Q}$ is the covariance associated with $\boldsymbol{w}$ in the discrete-time domain. $\bar{\boldsymbol{P}}$ contains each state's error variance along the diagonal:

$$\bar{\boldsymbol{P}} = \begin{bmatrix} \boldsymbol{\Sigma}_r & \bullet & \bullet & \bullet & \bullet \\ \bullet & \boldsymbol{\Sigma}_v & \bullet & \bullet & \bullet \\ \bullet & \bullet & \boldsymbol{\Sigma}_E & \bullet & \bullet \\ \bullet & \bullet & \bullet & \boldsymbol{\Sigma}_{ba} & \bullet \\ \bullet & \bullet & \bullet & \bullet & \boldsymbol{\Sigma}_{bg} \end{bmatrix}. \tag{8}$$

The position error standard deviation ($\mathbf{\Sigma}_r$) contains the error standard deviation of the along-track ($\sigma_x$), and that of the cross-track ($\sigma_y$ ). We compare the $\sigma_x$ and $\sigma_y$ to 0.1 meters, the maximum allowable position error standard deviation from the integrity requirement. $\bar{\boldsymbol{P}}$ is used for integrity evaluation rather than $\hat{\boldsymbol{P}}$ because $\bar{\boldsymbol{P}}$ will be available to the vehicle at the INS output rate, which will be higher than the GNSS output rate. Table 1 shows the sensor noise parameters used in our simulations.

| Sensor | Noise | Unit | Value | |
|---|---|---|---|---|
| INS | | | STIM300<br>Tactical grade | Ellipse2<br>Industrial grade |
| Accelerometer | Velocity Random Walk ($1\sigma$) | m/s/$\sqrt{\text{hr}}$ | 0.07 | 0.033 |
| | Bias Stability ($1\sigma$) | mg | 0.05 | 0.014 |
| | Bias Time Constant | hr | (1) | (1) |
| | Bias repeatability ($1\sigma_0$) | mg | 0.75 | - |
| Gyro | Angular Random Walk ($1\sigma$) | deg/$\sqrt{\text{hr}}$ | 0.15 | 0.15 |
| | Bias Stability ($1\sigma$) | deg/hr | 0.5 | 7 |
| | Bias Bias Time Constant | hr | (1) | (1) |
| | Bias repeatability ($1\sigma_0$) | deg/hr | 4 | - |
| Zero Velocity | Violation Noise ($1\sigma$) | m/s | 0.001 | |
| LiDAR | Ranging ($1\sigma$) | m | 0.01 | |
| | Angle ($1\sigma$) | deg | 0.3 | |
| | Survey ($1\sigma$) | m | 0.02 | |
| GNSS | Carrier Thermal Noise ($1\sigma$) | m | 0.001 | |
| | Code Thermal Noise ($1\sigma$) | m | 0.25 | |
| | Carrier Multipath ($1\sigma$) | m | 0.005 | |
| | Code Multipath ($1\sigma$) | m | 0.5 | |
| | Carrier Multipath Time Constant | s | 150 | |
| | Code Multipath Time Constant | s | 80 | |
| Speed Sensor | Measurement Noise ($1\sigma$) | m/s | 0.05 | |

**Table 1:** Sensor noise parameters. Note: ( ) is the value used in the paper but not specified by the manufactures.

## IV. CRITICAL ELEMENTS OF URBAN NAVIGATION

### 1. Analytic INS Position Error Models

Integration with an INS extends continuity in urban environments, with the duration of extension varying with the INS quality, which is typically loosely characterized by ‘grade’. Unfortunately, a general grade categorization is not particularly useful as a quality guideline for the current application because of the other (non-GNSS) sensors and kinematic constraints in play, and because of the complex contributions of individual INS error characteristics. The outputs from accelerometers and gyros in an INS (specific forces and angular rates, respectively) are each subject to Gaussian white noise and slowly varying biases. Manufacturers specify these error sources in terms of random walk, bias stability, bias time constant, and bias repeatability noise parameters (Woodman, 2007). Random walk is additive Gaussian white noise on the accelerometer and gyro measurements, and bias stabilities and bias time constants of the accelerometers and gyros are typically used to model the biases themselves as first-order Gauss-Markov processes. The initial knowledge of the bias state is referred to as bias repeatability. Table 1 describes the INS noise parameters of STIM300 (tactical grade) and Ellipse2 (industrial grade).

The EKF algorithm automatically produces the best estimation by mixing these noise parameters together, but it makes the impact of the individual error source invisible. We show how much each INS error source contributes to the total position error by deriving analytic INS position error models and determine how fast these propagate during GNSS signal outages. The analysis aids in the selection of INS specialized for driverless vehicles.

We derive two analytic INS position error models considering the bias as a first-order Gauss-Markov process or as Gaussian white noise (dubbed precise and approximate, respectively). The derivations of the equations are given in the appendix. Assuming perfect initialization and alignment, the precise INS position error model is described as

$$\sigma_r = \sqrt{\left(\frac{Q_{\nu a}t^3}{3} + \sigma_{r1}^2 + \frac{g^2Q_{\nu g}t^5}{20} + g^2\sigma_{r2}^2\right.} \tag{9}$$

$$\sigma_{r1}^2 = \frac{Q_{\eta a}}{a^2}\left(-\frac{e^{-2at}}{2a^3} - \frac{2ate^{-at}}{a^3} + \frac{1}{2a^3} + \frac{t}{a^2} - \frac{t^2}{a} + \frac{t^3}{3}\right) \tag{10}$$

$$\sigma_{r2}^2 = \frac{Q_{\eta g}}{b^2} \quad \frac{\left(b^2t^2+2\right)e^{-bt}}{b^5} - \frac{e^{-2bt}}{2b^5} + \frac{t^5}{20} - \frac{t^4}{4b} + \frac{2t^3}{3b^2} - \frac{t^2}{b^3} + \frac{t}{b^4} - \frac{3}{2b^5}\Bigg)\Bigg( \tag{11}$$

where $Q_{\nu a}$ is the power spectral density (PSD) of accelerometer random walk, $Q_{\eta a}$ is the PSD of accelerometer bias stability, $Q_{\nu g}$ is the PSD of gyro random walk, and $Q_{\eta g}$ is the PSD of gyro bias stability, $g$ is gravity, $a$ is accelerometer bias time constant, and $b$ is gyro bias time constant. The approximate INS position error model is described as

$$\sigma_r = \sqrt{\left(\frac{Q_{\nu a}t^3}{3} + \frac{Q_{\eta a}t^5}{20} + \frac{g^2Q_{\nu g}t^5}{20} + \frac{g^2Q_{\eta g}t^7}{252}\right.}. \tag{12}$$

Figure 6 plots the STIM300 INS position error drift versus time using the two analytic INS position error models and the actual EKF results. The approximate INS position error model given by (12) produces the same results as the EKF within a few minutes minute and diverges from it after one hour. We will use (12) in the analysis in the remainder of this section because the INS position drift error reaches the 0.1-meter maximum allowable position error standard deviation within one minute.

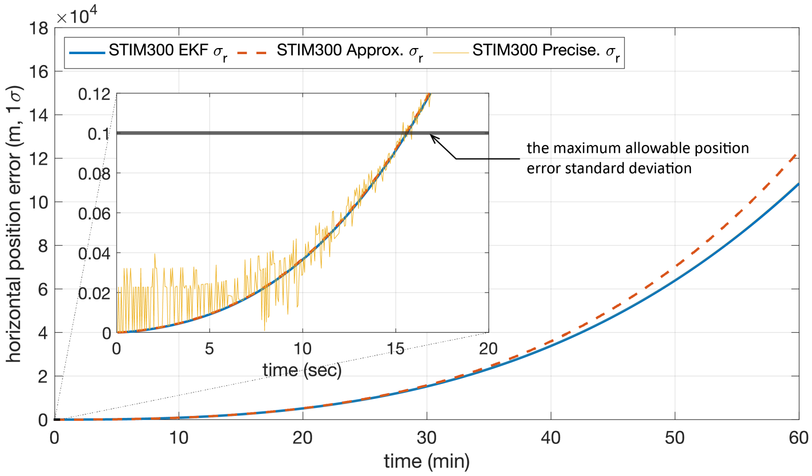

**Figure 6:** The STIM300 INS drifting position error versus time using the two analytic models and the EKF results.

Figure 7a shows the contribution of each STIM300 INS error source to the total position error and how fast each propagates under GNSS signal outages. The accelerometer and gyro random walks contribute the majority of the total position error at the beginning, but the gyro bias stability surpasses all other sources after after 1 hour. Although the bias stability of the Ellipse2 is 14 times larger than that of the STIM300, the error source still has less of an impact on the 0.1-meter maximum allowable position error standard deviation (Fig. 7b) than the gyro and accelerometer random walks, which are clearly revealed here to be the critical INS specifications for driverless vehicle applications.

Figure 8 compares the performance of three different INS grades showing the time when the position error drifts to the maximum allowable position error standard deviation after perfect initialization and alignment. The Ellipse2 performs the same as the STIM300 under the driverless car integrity requirements because both exceed the 0.1-meter position limit at around 15.5 seconds. The position drifting time examination enables INS selection by performance rather than grade, and it aids in INS cost optimization.

Of course, stricter requirements on specific INS noise parameters can help with endurance but will undoubtedly incur higher costs. They will nevertheless still be far from sufficient to control drift in dense urban environments. For example, the navigation grade INS (HG9900) can withstand 71 seconds of GNSS signal outage (Fig. 8), equivalent to 710 meters at 10 m/s vehicle

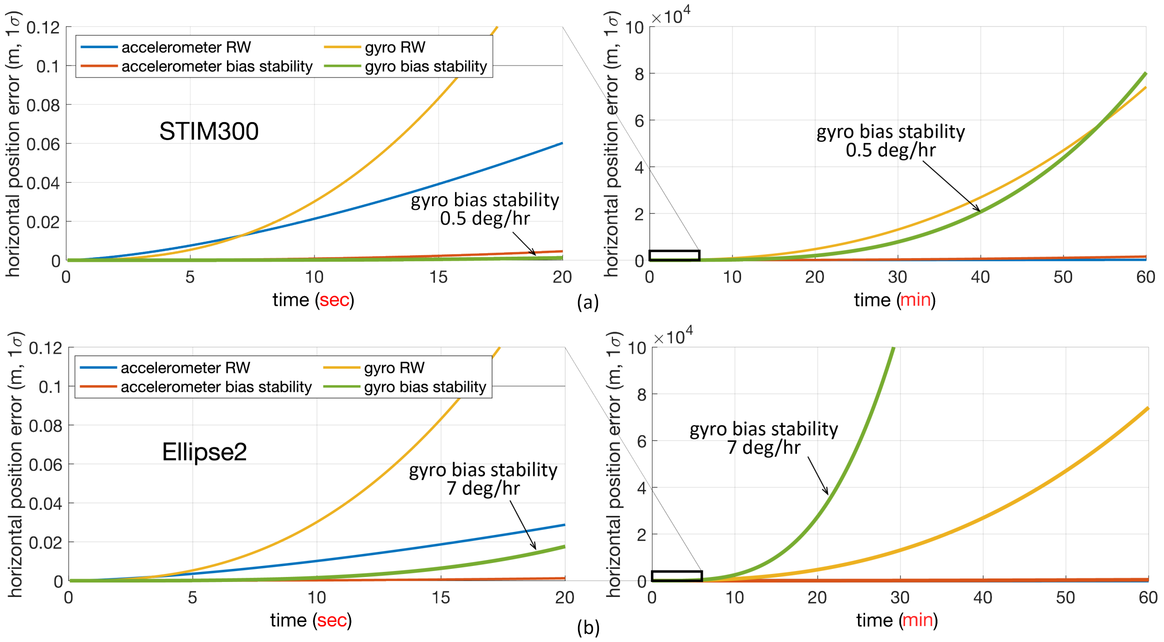

**Figure 7:** Error propagations of (a) each STIM300 INS error source, and (b) each Ellipse2 INS error source.

speed. Even neglecting the prohibitive cost of this sensor for the driverless car application, a succession of GNSS denied areas spanning several kilometers as in seen in Fig. 3 far exceeds 710 meters, so the navigation grade INS by itself would still be insufficient to bridge the GNSS signal outage.

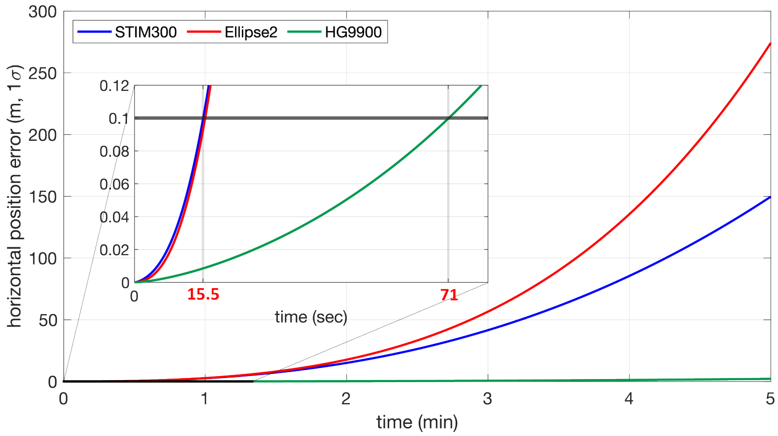

**Figure 8:** Performance boundary examination among three grades of INS.

## 2. Velocity Update

Frequent GNSS position reference updates, either via having more open sky areas or by traveling at higher speeds to more quickly reach the next open area, can mitigate INS position drift, but they are not controllable by a vehicle's positioning system. However, other dead reckoning sensors are also available to vehicles navigating urban environments. Wheel speed sensors can provide velocity updates consistently, and ZUPT is applicable when the system can identify stationary situations (Grejner-Brzezinska et al., 2002). We investigate how velocity updates slow down INS position error drift during GNSS signal outages, revealing the benefits and limitations of these additional sources of dead reckoning.

The EKF algorithm uses velocity information to improve position accuracy from the covariance between the position and velocity states. The position error after a velocity update $\sigma_{up}$ is related to the position error before velocity update $\sigma_r$, the correlation between position and velocity before velocity update $\sigma_{rv}$, and the velocity error before velocity update $\sigma_v$ by

$$\sigma_{up} = \sqrt{\left(\sigma_r^2 - \frac{\sigma_{rv}^4}{\sigma_v^2}\right.}. \tag{13}$$

The INS position error correction after velocity update is described as

$$\sigma_{up} = \sqrt{\left(\frac{Q_{\nu a} t^3}{12} + \frac{Q_{\eta a} t^5}{320} + \frac{g^2 Q_{\nu g} t^5}{320} + \frac{g^2 Q_{\eta g} t^7}{9072}\right.}, \tag{14}$$

where the time $t$ is referenced to the onset time of the GNSS outage. The derivations of the previous two results are provided in the appendix. In Table 2, equations (12) and (14) are used to produce the fractions expressing position error improvements following velocity updates for each INS noise parameter. The velocity update calibrates the position accuracy to some extent, but it does not reset the entire INS drifting position error. Additionally, the position error improvements by velocity updates are different for the individual INS noise parameters. For example, the position error generated by gyro bias stability is rduced by a factor of $1/6$ after the velocity update, while that by accelerometer random walk is $1/2$. Figure 9 shows the ZUPT position error corrections estimated by the EKF and equation (14). The position correction for the Ellipse2 is greater than that for the STIM300 due to the its higher gyro bias instability.

| | Velocity RW | Angler RW | Accelerometer Bias | Gyro Bias |
|---|---|---|---|---|
| $\sqrt{\left(\sigma_{up}^2\right.}$ | $\frac{\sigma_r}{2}$ | $\frac{\sigma_r}{4}$ | $\frac{\sigma_r}{4}$ | $\frac{\sigma_r}{6}$ |

**Table 2:** The fractions expressing position error improvements after velocity updates at each INS noise parameter. Note: $\sigma_r$ indicates the position error generated by each noise parameter before velocity update.

Velocity updates help the navigation system to bridge GNSS signal outages by calibrating position accuracy to some extent. However, position error will still accumulate over time without external position reference updates.

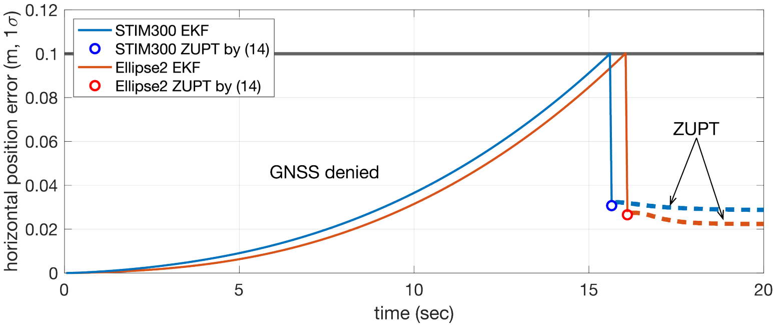

**Figure 9:** The position error corrections by ZUPT estimated by the EKF and by (14).

## 3. Position Reference Density

To regain control over navigation performance in urban environments, we consider augmentation by LiDAR ranging from local landmarks. A LiDAR sensor detects objects in the surrounding space and measures the ranges and angles to those within its field of view. The data points are associated with pre-defined landmarks that correspond to known locations on a map. The vehicle estimates its position using the mapped landmark locations and LiDAR measurements. Assuming landmarks can be added to existing environments, we can predict the necessary position reference density in future urban environments where navigation availability for driverless vehicles is essentially 100%.

We integrate LiDAR ranging from two different of landmark density assumptions: (1) traffic light poles already existing at intersections (e.g., every 200 meters) based on actual mapped locations, and (2) streetlight poles purposefully arranged every 35 meters. In either case, the navigation system uses one landmark at a time as an external position reference. As vehicle drives in the along-track direction as shown in Fig. 10 measurements are taken within ± 2 meters of the landmark. The simulation results in the following section show that position reference density is a major factor in maintaining fault-free integrity.

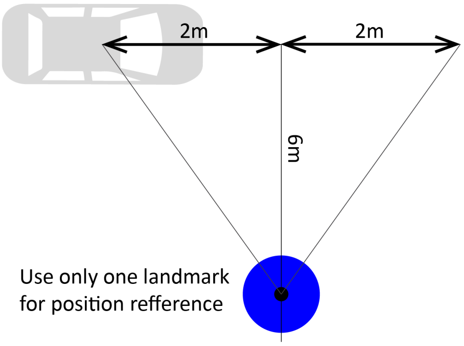

**Figure 10:** Configuration of the navigation system and a position reference landmark measured by LiDAR.

## V. SIMULATIONS

We simulate a driverless city bus traveling nine kilometers along State Street in Chicago from 35th Street in the south to North Avenue in the north. The bus route along the street passes through a variety of environments, ranging from low-rise, near open-sky neighborhoods to dense urban canyons with skyscrapers taller than 100 meters. High-definition 3D maps used in the simulation include all of the streets and buildings (Fig. 2a). The average bus speeds are examined by GPS traces received from Chicago Transit Authority buses in 2018 that vary with segments and time of day. We select a 5:00 pm commute time containing the slowest speed and assume the bus halts at all bus stops along the street for 20 seconds with deceleration or acceleration of 1 m/s$^2$ (Fig. 11). The results of six simulation scenarios are shown in Figures 12-16, which examine how navigation sensor integrations affect the integrity, continuity, and availability (Table 3).

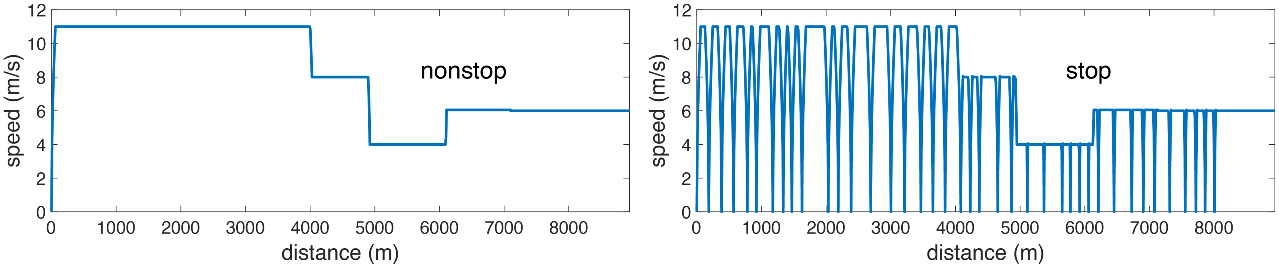

**Figure 11:** Bus speed: nonstop (left) and stop (right) scenarios.

| Figure | Speed | Sensors | INS | Position reference density |
|---|---|---|---|---|
| 12 | nonstop | INS, GNSS, WSS, NHL, HL | STIM300 | - |
| 13 | stop | INS, GNSS, WSS, NHL, HL | STIM300 | - |
| 14 | stop | INS, ZUPT, GNSS, WSS, NHL, HL | STIM300 | - |
| 15 | stop | INS, ZUPT, GNSS, WSS, NHL, HL | Ellipse2 | - |
| 16 | stop | INS, ZUPT, LiDAR, GNSS, WSS, NHL, HL | STIM300 | Intersection |
| 17 | stop | INS, ZUPT, LiDAR, GNSS, WSS, NHL, HL | STIM300 | Every 35 meters |

**Table 3:** The simulation scenarios and corresponding figures showing the navigation performance results

Each figure describes the one standard deviation of position error versus distance and includes the results for the along-track (left side, blue) and the cross-track directions (right side, red). The starting point is in open sky, and the environment gradually changes to deep urban canyons as the distance increases. The simulation is repeated every 15 minutes for 24 hours, and each thin gray line gives the fault-free integrity at that time. The upper bound of the set of integrity results indicates availability, and the navigation system provides 100% availability when the upper bound is less than 0.1 meters. The navigation performance of the cross-track direction is always superior to that of the along-track because of the effect of non-holonomic constraint.

The comparison of Figures 12 and 13 shows that a vehicle's speed strongly influence es fault-free integrity, and the navigation performance in the nonstop scenario is better than for the stop case as indicated between 3500 and 4500 meters. The INS

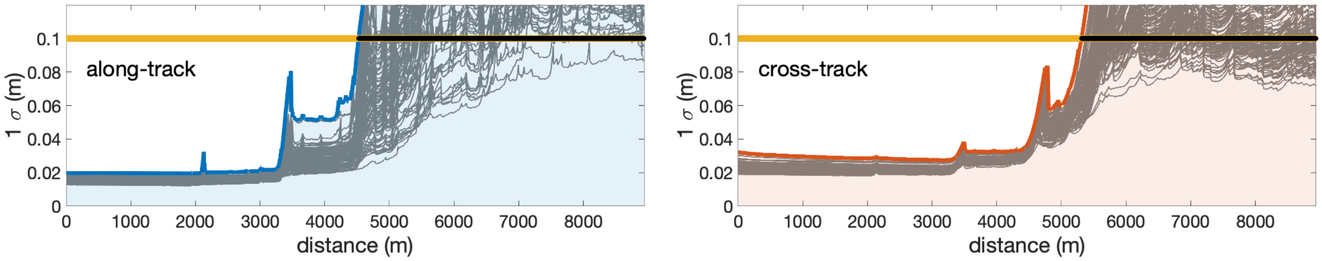

**Figure 12:** Navigation performance: nonstop / INS, GNSS, WSS, NHL, HL / STIM300

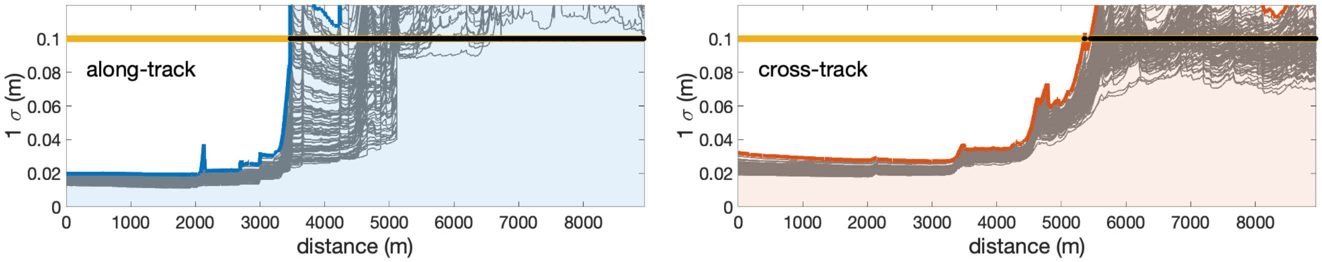

**Figure 13:** Navigation performance: stop / INS, GNSS, WSS, NHL, HL / STIM300

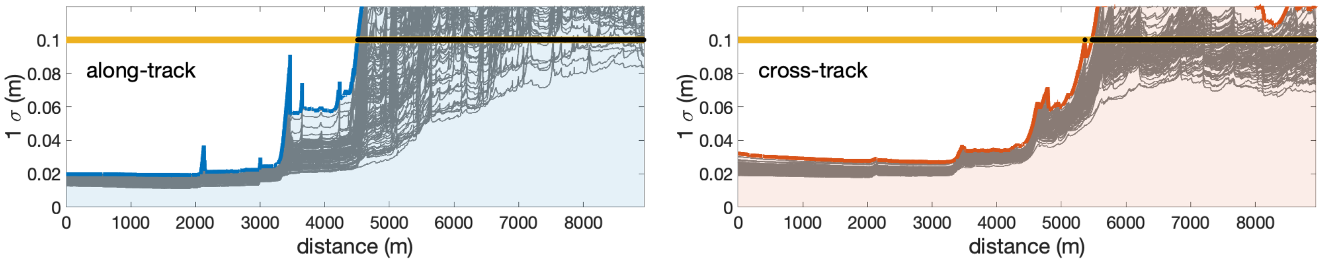

**Figure 14:** Navigation performance: stop / INS, ZUPT, GNSS, WSS, NHL, HL / STIM300

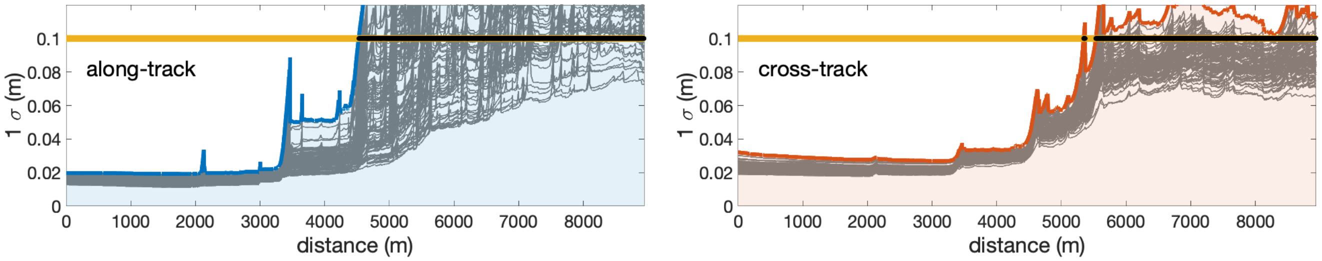

**Figure 15:** Navigation performance: stop / INS, ZUPT, GNSS, WSS, NHL, HL / Ellipse2

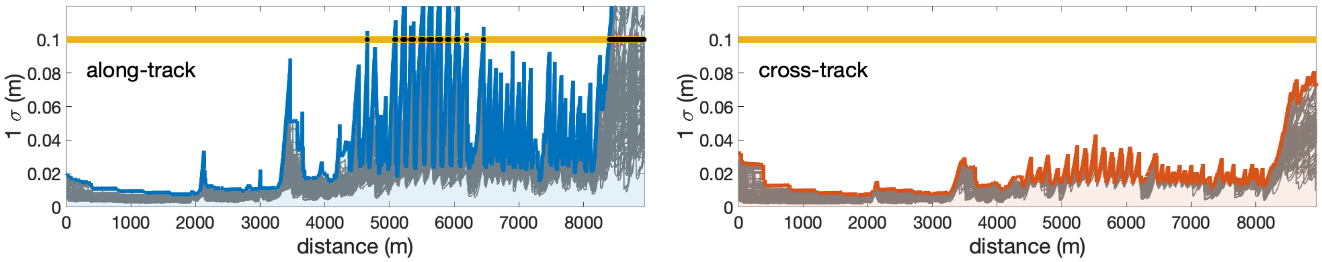

**Figure 16:** Navigation performance: stop / INS, ZUPT, LiDAR, GNSS, WSS, NHL, HL / STIM300 / Traffic light poles

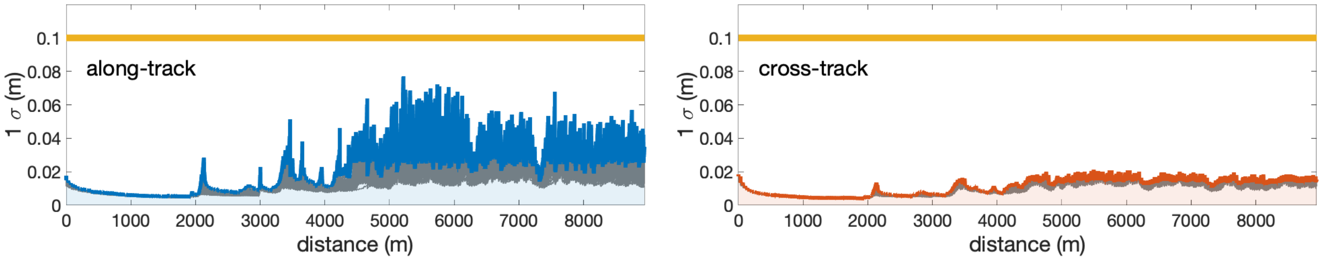

**Figure 17:** Navigation performance: stop / INS, ZUPT, LiDAR, GNSS, WSS, NHL, HL / STIM300 / Every 35 meters

drifting position error exceeds the 0.1-meter standard deviation when the vehicle slows down or stops in GNSS signal outage areas. Vehicle speed is not always controllable in urban environments (e.g., traffic lights, congestion, etc.), so we investigate ZUPT to calibrate the drifting position error during stationary vehicle situations.

Figures 12, 13, and 14 show that ZUPT recovers integrity to the same level as nonstop when the vehicle starts and stops repeatedly in GNSS compromised environments. The INS position error drifts when the vehicle stop coincides with a GNSS signal outage, but ZUPT calibrates the INS position error by using the stationary information. Deliberate vehicle stopping incorporating ZUPT extends navigation continuity if the vehicle is unable to travel at high speeds to a GNSS available area. But the need to decelerate and accelerate near stopping points lengthens the overall duration of the trip which increases the effects of inertial drift (as seen in Fig. 13) and tends to counteract the gains achieved by the ZUPT (leading to results in Figs. 12 and 14 that are nearly the same).

Figures 14 and 15 show results using the two grades of INS investigated earlier: the tactical grade STIM300 and industrial grade Ellipse2. Based on the the analysis in the last section it is not surprising that the performance results here are almost exactly the same for the two INS grades.

Figures 12 - 15 show that a navigation system comprised only of ‘conventional’ sensors (i.e., INS, ZUPT, GNSS, wheel speed sensors, non-holonomic, and holonomic kinematic constraints) do not maintain integrity through the city after 4500 meters. The conventional sensors can extend continuity where intermittent GNSS signals exist, between 3500 and 4500 meters, but cannot ensure availability after 4500 meters due to a succession of GNSS denied situations (Fig. 3).

Figure 16 shows the necessity of position reference updates in the succession of GNSS denied situations. The navigation system augmented by LiDAR ranging from traffic light poles already existing at intersections improves the navigation performance, but the integrity does not meet the requirements in some areas because of the lack of a needed position reference. Figure 17 shows that the position reference density required in urban environments to maintain navigation fault-free integrity is approximately one landmark every 35 meters (with INS, ZUPT, LiDAR, GNSS, wheel speed sensors, non-holonomic, and holonomic kinematic constraints).

The length of GNSS outages determines the necessary navigation sensors required for urban navigation. When GNSS position reference updates are not acquired before the position error exceeds the maximum allowable position error standard deviation, the system must be augmented by an alternative sensor providing position reference — in our case, LiDAR using local landmarks — allowing driverless vehicles to navigate safely (in the absence of faults) through urban areas.

## VI. CONCLUSION

We explore future navigation systems with the goal of achieving 100% availability for urban driverless vehicles. Our research begins by adopting integrity requirements for driverless vehicles under a fault-free scenario, which is a 0.1-meter maximum allowable position error standard deviation. We evaluate performance along a nine-kilometer-long urban transect in downtown Chicago, where availability using GNSS alone, as evaluated by compliance with the integrity requirement, falls far short of 100%. We then consider a multi-sensor integrated navigation architecture consisting of INS, ZUPT, GNSS, LiDAR, wheel speed sensors, non-holonomic, and holonomic kinematic constraints to extend navigation continuity. Investigation of individual INS noise source contributions reveals that accelerometer and gyro random walk contribute to the total position error much more than gyro bias stability under the driverless vehicle integrity requirement. Velocity updates can partially calibrate the position error but do not completely reset the INS drifting position errors. Intentional vehicle stops extend navigation continuity by ZUPT to the same level as the nonstop scenario. However, position reference updates are required for a succession of GNSS denied environments. The multi-sensor navigation system acquiring a position reference every 35 meters, in our case LiDAR ranging from local landmarks, achieves 100% navigation availability for driverless vehicles in the urban environment studied.

## REFERENCES

Brenner, C. (2009). Global localization of vehicles using local pole patterns. In *Joint Pattern Recognition Symposium*, pages 61–70. Springer.

Chapman, L., Thornes, J. E., and Bradley, A. V. (2002). Sky-view factor approximation using GPS receivers. *International Journal of Climatology: A Journal of the Royal Meteorological Society*, 22(5):615–621.

Cosmen-Schortmann, J., Azaola-Sáenz, M., Martinez-Olague, M., and Toledo-López, M. (2008). Integrity in urban and road environments and its use in liability critical applications. In *2008 IEEE/ION Position, Location and Navigation Symposium*, pages 972–983. IEEE.

Davis, J. M. and Kelly, R. J. (1993). RNP tunnel concept for precision approach with GNSS application. In *Proceedings of the 49th Annual Meeting of The Institute of Navigation (1993)*, pages 135–154.

Falco, G., Pini, M., and Marucco, G. (2017). Loose and tight GNSS/INS integrations: Comparison of performance assessed in real urban scenarios. *Sensors*, 17(2):255.

Gao, J., Petovello, M. G., and Cannon, M. E. (2007). GPS/low-cost IMU/onboard vehicle sensors integrated land vehicle positioning system. *EURASIP Journal on Embedded Systems*, 2007:1–14.

Grejner-Brzezinska, D. A., Toth, C. K., and Yi, Y. (2002). Bridging GPS gaps in urban canyons: Can ZUPT really help? In *Proceedings of the 58th Annual Meeting of The Institute of Navigation and CIGTF 21st Guidance Test Symposium (2002)*, pages 231–240.

Groves, P. D. (2011). Shadow matching: A new GNSS positioning technique for urban canyons. *The journal of Navigation*, 64(3):417–430.

Householder, A. S. (1958). Unitary triangularization of a nonsymmetric matrix. *Journal of the ACM (JACM)*, 5(4):339–342.

Nagai, K., Fasoro, T., Spenko, M., Henderson, R., and Pervan, B. (2020). Evaluating gnss navigation availability in 3-d mapped urban environments. In *2020 IEEE/ION Position, Location and Navigation Symposium (PLANS)*, pages 639–646. IEEE.

Nagai, K., Spenko, M., Henderson, R., and Pervan, B. (2021a). Evaluating INS/GNSS availability for self-driving cars in urban environments. In *Proceedings of the 2021 International Technical Meeting of The Institute of Navigation*, pages 243–253.

Nagai, K., Spenko, M., Henderson, R., and Pervan, B. (2021b). Evaluating INS/GNSS/LiDAR availability for self-driving cars in urban environments. In *Proceedings of the 34th International Technical Meeting of the Satellite Division of The Institute of Navigation (ION GNSS+ 2021)*, pages 2121–2132.

Obst, M., Bauer, S., and Wanielik, G. (2012). Urban multipath detection and mitigation with dynamic 3D maps for reliable land vehicle localization. In *Proceedings of the 2012 IEEE/ION Position, Location and Navigation Symposium*, pages 685–691. IEEE.

Reid, T. G., Houts, S. E., Cammarata, R., Mills, G., Agarwal, S., Vora, A., and Pandey, G. (2019). Localization requirements for autonomous vehicles. *SAE International Journal of Connected and Automated Vehicles*, 2(3):1–16.

Tanil, C. (2016). *Detecting GNSS spoofing attacks using INS coupling*. Illinois Institute of Technology.

Titterton, D., Weston, J., Weston, J., of Electrical Engineers, I., of Aeronautics, A. I., and Astronautics (2004). *Strapdown Inertial Navigation Technology*. IEE Radar Series. Institution of Engineering and Technology.

Woodman, O. J. (2007). An introduction to inertial navigation. Technical report, University of Cambridge, Computer Laboratory.

Zhu, N., Marais, J., Bétaille, D., and Berbineau, M. (2018). GNSS position integrity in urban environments: A review of literature. *IEEE Transactions on Intelligent Transportation Systems*, 19(9):2762–2778.

## APPENDIX A: ANALYTIC INS POSITION ERROR MODELS

The acceleration of the INS mechanization (Tanil, 2016), when the specific force and the alignment are zero, is described in the following equation.

$$\delta\dot{\boldsymbol{v}}_N = \underbrace{-2{}^I\boldsymbol{\omega}_N^E \times \delta\boldsymbol{v}_N}_{\approx 0} + {}^N\mathbf{R}^{B*}\boldsymbol{f}_B^* \times \delta\boldsymbol{E} - {}^N\mathbf{R}^{B*}\mathbf{b}_a + \underbrace{{}^N\mathbf{R}^{B*}\delta\tilde{\mathbf{f}}_B}_{\approx 0} - {}^N\mathbf{R}^{B*}\boldsymbol{\nu}_a \approx \underbrace{\boldsymbol{f}_B^* \times \delta\boldsymbol{E}}_{\text{gyro noise}} - \underbrace{\mathbf{b}_a}_{\text{bias}} - \underbrace{\boldsymbol{\nu}_a}_{\text{white noise}} \tag{15}$$

The gyro noise part of the horizontal direction is $g\theta_{err}$ (horizontal), and that of the vertical is 0 (vertical) because of the matrix calculation.

$$\boldsymbol{f}_B^* \times \delta\boldsymbol{E} = \begin{bmatrix} 0 \\ 0 \\ g \end{bmatrix} \times \begin{bmatrix} \delta_\phi \\ \delta_\theta \\ \delta_\psi \end{bmatrix} = \begin{bmatrix} -g\delta_\theta \\ g\delta_\phi \\ 0. \end{bmatrix} \tag{16}$$

The angler rate of the INS mechanization is described as

$$\delta\dot{\boldsymbol{E}}_N = \underbrace{\boldsymbol{K}^*\delta\boldsymbol{E}_N}_{\approx 0} - \boldsymbol{Q}_{be}^{-1}\mathbf{b}_g + \underbrace{\boldsymbol{Q}_{be}^{-1}\delta^I\tilde{\boldsymbol{\omega}}_B^B}_{\approx 0} - \boldsymbol{Q}_{be}^{-1}\boldsymbol{\nu}_g \approx -\underbrace{\mathbf{b}_g}_{\text{bias}} - \underbrace{\boldsymbol{\nu}_g}_{\text{white noise}} \quad . \tag{17}$$

The integral of (17) is

$$\delta E_N = \theta_{err} = -\int_0^t b_g \, d\tau - \int_0^t \nu_g d\tau. \tag{18}$$

From (15) to (18), the acceleration equation obtains

$$\delta\dot{v}_N = g\int_0^t b_g \, d\tau + g\int_0^t \nu_g d\tau - b_a - \nu_a. \tag{19}$$

The position, the integrals of the acceleration, is formed as

$$\delta r_N = g\int_0^t\int_0^s\int_0^r b_g d\tau dr ds + g\int_0^t\int_0^s\int_0^r \nu_g d\tau dr ds - \int_0^t\int_0^s b_a d\tau ds - \int_0^t\int_0^s \nu_a d\tau ds. \tag{20}$$

When the bias is expressed by Gaussian white noise, the equation is

$$\dot{b}_a = -\frac{1}{\tau_a} b_a + \eta_a \approx \eta_a \tag{21}$$

$$b_a = \int_0^t \eta_a \, d\tau. \tag{22}$$

From (20) and (22), the position with approximated bias equation becomes

$$\delta r_N = g\int_0^t\int_0^s\int_0^r\int_0^q \eta_g \, d\tau dq dr ds + g\int_0^t\int_0^s\int_0^r \nu_g d\tau dr ds - \int_0^t\int_0^s\int_0^r \eta_a \, d\tau dr ds - \int_0^t\int_0^s \nu_a d\tau ds. \tag{23}$$

Sensor noise can be described by both frequency and time domains with Power Spectral Density (PSD).

$$\sigma^2 = Q\int_{-\infty}^{\infty} |H(f)|^2 df = Q\int_0^t h(\tau)^2 d\tau \tag{24}$$

The integral of white noise in the time domain can be described as

$$h_0(t) = \delta(t) = \infty \tag{25}$$

$$h_1(t) = \int_0^t h_0(\tau)d\tau = 1 \tag{26}$$

$$h_2(t) = \int_0^t \int_0^s h_0(\tau)d\tau ds = t \tag{27}$$

$$h_3(t) = \int_0^t \int_0^s \int_0^r h_0(\tau)d\tau dr ds = \frac{t^2}{2} \tag{28}$$

$$h_4(t) = \int_0^t \int_0^s \int_0^r \int_0^q h_0(\tau)d\tau dq dr ds = \frac{t^3}{6}. \tag{29}$$

From (23), (27), (28), and (29), the analytic horizontal position error model becomes

$$\sigma_r^2 = Q_{\nu a}\int_0^t h_2(\tau)^2 d\tau + Q_{\eta a}\int_0^t h_3(\tau)^2 d\tau + g^2 Q_{\nu g}\int_0^t h_3(\tau)^2 d\tau + g^2 Q_{\eta g}\int_0^t h_4(\tau)^2 d\tau \tag{30}$$

$$= Q_{\nu a}\int_0^t \tau^2 d\tau + Q_{\eta a}\int_0^t \left(\frac{\tau^2}{2}\right)^2 d\tau + g^2 Q_{\nu g}\int_0^t \left(\frac{\tau^2}{2}\right)^2 d\tau + g^2 Q_{\eta g}\int_0^t \left(\frac{\tau^3}{6}\right)^2 d\tau \tag{31}$$

$$= \frac{Q_{\nu a}t^3}{3} + \frac{Q_{\eta a}t^5}{20} + \frac{g^2 Q_{\nu g}t^5}{20} + \frac{g^2 Q_{\eta g}t^7}{252} \tag{32}$$

where

$\sigma_r$: horizontal position INS drift error

$Q_{\nu a}$: PSD of accelerometer white noise $((\mathrm{m/s^2})/\sqrt{\mathrm{Hz}})^2$

$Q_{\eta a}$: PSD of accelerometer bias stability white noise $((\mathrm{m/s^3})/\sqrt{\mathrm{Hz}})^2$

$Q_{\nu g}$: PSD of gyro white noise $((\mathrm{rad/s})/\sqrt{\mathrm{Hz}})^2$

$Q_{\eta g}$: PSD of gyro bias stability white noise $((\mathrm{rad/s^2})/\sqrt{\mathrm{Hz}})^2$

$g$: gravity.

When the bias is expressed by the first-order Gauss-Markov process, the equation is

$$\dot{b}_a = -\frac{1}{\tau_a} b_a + \eta_a = -a b_a + \eta_a. \tag{33}$$

The Laplace transform is

$$b_a(S) = \underbrace{\frac{1}{S+a}}_{H(s)} \eta_a(S). \tag{34}$$

(34) can be described in the time domain. The integral becomes

$$h_0(t) = e^{-at} \tag{35}$$

$$h_1(t) = \int_0^t h_0(\tau)d\tau = \frac{1}{a}(1 - e^{-at}) \tag{36}$$

$$h_2(t) = \int_0^t \int_0^s h_0(\tau)d\tau ds = \frac{1}{a}\left(\frac{e^{-at}}{a} + t - \frac{1}{a}\right) \tag{37}$$

$$h_3(t) = \int_0^t \int_0^s \int_0^r h_0(\tau)d\tau dr ds = \frac{1}{a}\left(-\frac{e^{-at}}{a^2} + \frac{t^2}{2} - \frac{t}{a} + \frac{1}{a^2}\right) \tag{38}$$

$$\tag{39}$$

The integration of bias noise expressed by the first-order Gauss-Markov process becomes

$$\int_0^t b_a d\tau = Q\int_0^t h_1(\tau)^2 d\tau = \frac{Q}{a^2}\left(\frac{2e^{-at}}{a} - \frac{e^{-2at}}{2a} + t - \frac{3}{2a}\right) \tag{40}$$

$$\int_0^t\int_0^s b_a d\tau ds = Q\int_0^t h_2(\tau)^2 d\tau = \frac{Q}{a^2}\left(-\frac{e^{-2at}}{2a^3} - \frac{2ate^{-at}}{a^3} + \frac{1}{2a^3} + \frac{t}{a^2} - \frac{t^2}{a} + \frac{t^3}{3}\right) \tag{41}$$

$$\int_0^t\int_0^s\int_0^r b_a d\tau dr ds = Q\int_0^t h_3(\tau)^2 d\tau = \frac{Q}{a^2}\left(\frac{(a^2t^2+2)\mathrm{e}^{-at}}{a^5} - \frac{\mathrm{e}^{-2at}}{2a^5} + \frac{t^5}{20} - \frac{t^4}{4a} + \frac{2t^3}{3a^2} - \frac{t^2}{a^3} + \frac{t}{a^4} - \frac{3}{2a^5}\right) \tag{42}$$

From (20), (27), (28), (41), and (42), the analytic horizontal position error model becomes

$$\sigma_r^2 = \frac{Q_{\nu a}t^3}{3} + \sigma_{r1}^2 + \frac{g^2 Q_{\nu g}t^5}{20} + g^2\sigma_{r2}^2 \tag{43}$$

$$\sigma_{r1}^2 = \frac{Q_{\eta a}}{a^2}\left(-\frac{e^{-2at}}{2a^3} - \frac{2ate^{-at}}{a^3} + \frac{1}{2a^3} + \frac{t}{a^2} - \frac{t^2}{a} + \frac{t^3}{3}\right) \tag{44}$$

$$\sigma_{r2}^2 = \frac{Q_{\eta g}}{b^2}\left(\frac{(b^2t^2+2)\,e^{-bt}}{b^5} - \frac{\mathrm{e}^{-2bt}}{2b^5} + \frac{t^5}{20} - \frac{t^4}{4b} + \frac{2t^3}{3b^2} - \frac{t^2}{b^3} + \frac{t}{b^4} - \frac{3}{2b^5}\right) \tag{45}$$

where

$a$ : $\frac{1}{\tau_a}$, inverse of accelerometer bias time constant

$b$ : $\frac{1}{\tau_g}$, inverse of gyro bias time constant.

## APPENDIX B: THE INS POSITION ERROR CORRECTION BY VELOCITY UPDATE

The EKF algorithm improves position standard deviations with velocity information from covariance between position and velocity. The analytically derived equation is

$$\sigma_{up}^2 = \sigma_r^2 - \frac{\sigma_{rv}^2\sigma_{rv}^2}{\sigma_v^2}. \tag{46}$$

From (23), the velocity and position errors generated by the velocity random walk white noise are expressed

$$\sigma_v^2 = Q_{\nu a}\int_{-\infty}^{\infty} h_1(\tau)^2 d\tau = Q_{\nu a}t \tag{47}$$

$$\sigma_r^2 = Q_{\nu a}\int_{-\infty}^{\infty} h_2(\tau)^2 d\tau = \frac{Q_{\nu a}t^3}{3}. \tag{48}$$

From (47) and (48), the covariance between the velocity and position becomes

$$\sigma_{rv}^2 = Q_{\nu a}\int_{-\infty}^{\infty} h_1(\tau)h_2(\tau) d\tau = \frac{Q_{\nu a}t^2}{2} \tag{49}$$

By applying (47), (48), and (49) into (46), and the position correction by velocity update related to the velocity random walk white noise becomes

$$\sigma_{up}^2 = \frac{Q_{\nu a}t^3}{12}. \tag{50}$$

By comparing (32) and (50), the fraction of position error updated by velocity information related to the velocity random walk white noise becomes

$$\sigma_{up} = \frac{\sigma_r}{2}. \tag{51}$$

The position errors of the other noise parameters updated by velocity information can be derived in the same manner.